Shape resonances in the absolute *K*-shell photodetachment of B^-

N. Berrah,[1] R. C. Bilodeau,[1,2,*] I. Dumitriu,[1,2] J. D. Bozek,[2,†] N. D. Gibson,[3] C. W. Walter,[3] G. D. Ackerman,[2] O. Zatsarinny,[1,‡] and T. W. Gorczyca[1]

[1]*Department of Physics, Western Michigan University, Kalamazoo, Michigan 49008, USA*

[2]*Lawrence Berkeley National Laboratory, Advanced Light Source, Berkeley, California 94720, USA*

[3]*Department of Physics and Astronomy, Denison University, Granville, Ohio 43023, USA*

(Received 28 November 2006; revised manuscript received 16 July 2007; published 20 September 2007)

K-shell photodetachment of B^- has been measured using the collinear photon-ion beamline at the Advanced Light Source, Lawrence Berkeley National Laboratory, as well as calculated using two separate *R*-matrix methods. The measurement of the absolute photodetachment cross section, as a function of photon energy, exhibits three near-threshold shape resonances due to the ^3S, ^3P, and ^3D final partial waves. A fit to the measured data using three resonance profiles shows good overall qualitative agreement with the three partial wave cross sections calculated using either *R*-matrix method. However, certain significant and unresolved quantitative discrepancies exist between the experimentally inferred and the calculated resonance profiles.

DOI: 10.1103/PhysRevA.76.032713 PACS number(s): 32.80.Gc, 32.80.Hd

I. INTRODUCTION

Investigation of electron dynamics in negative ions provides valuable insight into the general problem of correlated motion of electrons of many-particle systems such as heavy atoms, molecules, clusters, and solids. In addition, studies of the properties of ions are needed to understand better dilute plasmas appearing on the outer atmosphere of stars. Photoexcitation and photodetachment processes of negative ions stand out as extremely sensitive probes and theoretical test beds for the important effects of electron-electron correlation because of the weak coupling between the photodetached electron and the neutral target states.

Negative ions are special targets since they contain confined electrons but do not exhibit Rydberg series, like neutral targets or positive ions, because the photodetached electron does not experience the long range Coulomb force. In fact, negative ions often exist only because of electron-electron correlation. The static potential seen by the outermost electron is often insufficient to bind another electron, and instead higher order contributions are responsible for the binding of the electron. Theoretical studies have demonstrated that it is necessary to include both core-valence and core-core effects since it leads to much better agreement with experiments [1].

From an experimental point of view, inner-shell photodetachment experiments, unlike the numerous outer-shell studies as described in the reviews by Buckman *et al.* [2] and Andersen [3], were initiated only recently, by two independent research groups [4,5] and were thus a relatively unexplored territory as of 2001. The past few years, however, have witnessed tremendous activity in inner-shell negative-ion photodetachment, both experimentally [4–18] and theoretically [19–27]. Inner-shell photodetachment studies of light elements such as He^- [8,13,15,19,23–25], Li^- [4,5,20,26], C^- [9,18,27] and F^- [14] have reported resonance structure *and* absolute cross section behavior (see also the recent review by Kjeldsen [28]).

In this work, we report on measurements of the resonance structure and absolute cross sections for the *K*-shell photodetachment of B^- and compare them to two *R*-matrix calculations. The specific process of interest is the following:

$$h\nu + \mathrm{B}^-\left(1s^2 2s^2\left[2p^2(^3P)\right]\right)$$

$$\downarrow$$

$$\left\{\mathrm{B}^*\left(1s2s^2 2p^2\left[^4P,^2P,^2D,^2S\right]\right)\epsilon p\right\}\left(^3S,^3P,^3D\right)$$

$$\downarrow$$

$$\mathrm{B}^+\left(1s^2 2l2l'\right)\epsilon p\epsilon l\ . \tag{1}$$

K-shell photodetachment of B^- produces a *p*-wave photoelectron ϵp departing from a *K*-shell-vacancy $1s2s^22p^2$ state of B^* that subsequently undergoes Auger decay, producing a second, Auger electron ϵl and a B^+ ion; the latter is detected in the present experiment. We note that if $2p^2(^3P)$ core rearrangement, via interchannel continuum coupling, is neglected in Eq. (1), then only the ^4P and ^2P final states of B^* are populated.

The motivation for this work stems from the fact that *K*-shell photodetachment cross sections of He^-, Li^-, and C^- showed pronounced structures such as triply excited, Feshbach, and shape resonances. Here we provide additional results on *K*-shell photodetachment of a different light negative ion whose atomic number lies in between those already explored, thus allowing a systematic study of resonance structure in addition to providing absolute photodetachment cross sections. One clear qualitative difference is that *three* final partial waves result from the *K*-shell photodetachment of B^-, compared to the single final partial wave in the neighboring Li^- [4,5,20,26] or C^- [9,18,27] ions.

*rcbilodeau@lbl.gov

†Present Address: LCLS, Stanford Linear Accelerator Center, Menlo Park, CA 94025, USA.

‡Present Address: Department of Physics and Astronomy, Drake University, Des Moines, IA 50311, USA.

II. EXPERIMENTAL METHOD

The experiments were performed using the Ion-Photon beamline (IPB) [29] in tandem with the High-Resolution Atomic Molecular and Optical (HRAMO) undulator beamline 10.0.1. at the Advanced Light Source synchrotron radiation facility at Lawrence Berkeley National Laboratory. The IPB uses the merged beams technique for tunable spectroscopy with synchrotron radiation. Positive ions resulting from photoionization of the primary beam ions are detected with an energy analyzer. In the present study, B^- ions were produced using a cesium sputtering ion source (SNICS II) [30] accelerated to about 8.5 keV, and mass selected using a 60° sector magnet. The ion beam was deflected by 90° using a spherical electrostatic deflector to merge it with the counter-propagating photon beam. The ions were merged collinearly with the counter-propagating photon beam in a 29.4 cm long energy-tagged interaction region producing photodetached neutral B atoms and B^+ ions. After passing through the interaction region, the B^+ ions were deflected out of the primary beam with a demerging electromagnet, then passed through an electrostatic deflector to a microchannel plate-based detector. The bending magnet also directed the primary B^- beam into a Faraday cup to measure the ion current. Typical final primary beam currents after shaping and spatial trimming were about 100 nA. Only the B^+ ions were detected as a function of photon energy.

The photon energy was scanned using a grazing-incidence spherical-grating monochromator, and the positive ion production as a function of photon energy was recorded. The high resolution photodetachment data were acquired using a nominal photon bandwidth of 63 meV based on the monochromator slit settings, while the low-resolution data were obtained with 390 meV photon bandwidth. The photon flux was determined by measuring the current produced from an absolutely calibrated silicon photodiode. In order to discriminate against positive ions produced by stripping of the negative ions by background gas, the photon beam was chopped at 6 Hz. An integrated dwell time of 2 s was spent at each photon energy with the photons incident on the ions, and another 2 s was spent acquiring background data with the photon beam blocked. The photodetachment signal was determined by subtracting the photons-off signal from the photons-on signal. The resulting signal was normalized to the primary B^- ion beam and the incident photon flux. The photon energy was calibrated against accurately known absorption lines in Ar ($4s$ line at 244.39 eV) [31] and SF_6 (two lines at 183.4 and 184.57 eV) [32] using data from a previous run.

In order to determine absolute cross sections, it is necessary to accurately measure the geometrical overlap of the ion and photon beams. The beam profiles and overlaps were determined using a series of three monitors: two rotating wire beam profile monitors near the entrance and the exit of the interaction region and a translating-slit scanner in the middle of the interaction region. The outputs of each of these monitors were recorded under computer control to yield the two-dimensional profiles of the ion and photon beams. The overlap integral of the two beams was then determined by interpolating the overlap measured at each of the monitors over the entire interaction region length. All three monitors were removed from the beam path during data collection. Details of the methodology to measure absolute photodetachment cross sections are described elsewhere [13,29].

All the experimental data represented herein have been Doppler corrected to obtain the ion-frame photon energy. The total uncertainty for photon energy calibration, including Doppler correction, is estimated to be 50 meV [uncertainties are quoted to 1 standard deviation (SD) everywhere].

III. THEORETICAL METHODS

Two *R*-matrix methods were used to compare to the experimental photodetachment measurements. One of them was carried out with a computer program BSR [33] that we will refer to in the remainder of the manuscript as Theory I (ThI). The key feature of this approach is a significant improvement to the target description by using compact configuration-interaction expansions involving nonorthogonal sets of term-dependent one-electron orbitals. For the inner-core photodetachment of B^-, specifically, this method allows for the use of various $1s$ orbitals, thereby allowing for relaxation effects in the $1s$-vacancy states.

The close-coupling expansion included 25 bound and autoionizing states of neutral B derived from the $1s^22s^22p$, $1s^22s2p^2$, and $1s^22p^3$ configurations, plus the $1s2s^22p^2$, $1s2s2p^3$, and $1s2p^4$ configurations for $1s$ photodetachment. Emphasis was placed on the accuracy of target wave functions by using nonorthogonal orbitals. Each state (including the initial B^- state) was described by a different set of orbitals that were separately determined from state-specific multiconfiguration Hartree-Fock calculations [34]. The set of orbitals included the $1s$, $2s$, and $2p$ physical orbitals as well as $n=3$ and $n=4$ correlation orbitals. All single and double promotion configurations were used to construct the target expansions. They also included the promotion from the $1s$ shell that is important for an accurate determination of the relative position of the $1s$ vacancy states. Note that the initial $B(1s^22s^22p^2\ ^3P)$ state was obtained from a separate MCHF calculation, in contrast to standard *R*-matrix calculations where the initial state is usually described by the same close-coupling expansion as is used for the final continuum states.

For the initial state, we used the same number of physical and correlation orbitals as for the target states, and the resulting electron affinity of 0.276 eV closely agrees with the experimental value of 0.279723(25) eV [35]. The scattering calculations for the final continuum states were carried out with an *R*-matrix code [33], in which a B-spline basis is used to represent the continuum functions in the internal region. The total $(N+1)$-electron function is expanded in terms of energy-independent basis functions

$$\Psi_k = \mathcal{A}\sum_{ij} a_{ijk}\bar{\Phi}_i B_j(r) \quad 0 < r < a. \tag{2}$$

Here $\bar{\Phi}_i$ denote channel functions formed from the *N*-electron target states included in the close-coupling expansion, $B_j(r)$ are B-splines used to describe the scattering electron, and $\mathcal{A}$ is an antisymmetrization operator. Note that

there are no $(N+1)$-electron bound configurations included in the expansion of Eq. (2). Such terms are usually included in standard *R*-matrix calculations to compensate for the orthogonality constraints imposed on the continuum orbitals. We impose only very limited orthogonality constraints that do not affect the completeness of the total trial wave function. Specifically, in the present work, the scattering orbitals were constrained to be orthogonal only to the $1s$ and $2s$ core orbitals.

The coefficients a_{ijk} in Eq. (2) are determined by diagonalizing the $(N+1)$-electron Hamiltonian inside the *R*-matrix box. Using the B-spline basis leads to a generalized eigenvalue problem of the form

$$\mathbf{Hc} = E\mathbf{Sc}, \tag{3}$$

where **H** is the Hamiltonian matrix, **S** is the matrix of overlap integrals between individual B-splines, and columns of the matrix *c* are eigenvectors representing the B-spline amplitudes. In order to ensure hermiticity of **H** in the internal region, we add the Bloch operator [36]. The amplitudes of the wave functions at the boundary, that are needed to construct the *R* matrix, are given by the coefficients of the last spline—the only nonzero spline at the boundary. We used 113 B splines of order 8 with a semi-exponential grid of knots. An *R*-matrix radius of $a=40$ a.u. is used in order to contain the bound orbitals, and the scattering parameters were found by matching the inner solution at $r=a$ to the asymptotic solutions in the outer region, that were determined using the program ASYPCK [37].

The second theoretical method (ThII) is based on the standard, orthogonal-orbital *R*-matrix method [38] as implemented in the RmaX suite of codes [39]. While this is equivalent to the first method in principle, there are certain practical differences between the two approaches. Most importantly, the ThII method is restricted to the use of a single set of orbitals for describing each B^-, B^*, and/or B state. Thus a lot of extra configuration interaction (CI) is needed just to account for the strong relaxation effects that exist due to $1s$, $2s$, and $2p$ electron promotions in going from the $1s^22s^22p^2$ ground state of B^- to the $1s2s^22p^3$ intermediate shape-resonance states of B^{-*} to the $1s2s^22p^2+e^-$ final decay channels of B^* plus an electron. The ThI *R*-matrix method, on the other hand, accounts for such relaxation effects in lowest order. Thus, we expect that the full CI wave functions, and therefore the computed cross sections, are described more accurately by the ThI method than by the orthogonal-orbital ThII method.

For the present case, the ThII $1s$, $2s$, and $2p$ orbitals were determined from a Hartree-Fock calculation for the B $1s^22s^22p(^2P)$ state, and additional $\overline{3s}$, $\overline{3p}$, and $\overline{3d}$ pseudo-orbitals were determined from a MCHF calculation optimized on the inner-shell excited $1s2s^22p^2(^4P)$ state. All single and double promotions from the $n=2$ configurations were then included in the configuration expansion for the same 25 states of B that were included in the first method.

Another major difference between the two theoretical methods is that the ThII method requires additional bound-type B^- configurations in the close-coupling expansion to compensate for the enforced orthogonality of scattering to bound orbitals. In the present study, it was crucial to include only those required configurations for the final ^3S, ^3P, ^3D symmetries, which was accomplished using a pseudoresonance elimination technique [40] to choose the correct expansion of B^- configurations. When this elimination was not performed, an imbalance between the correlation in the neutral and anion states occurred, and the B^- resonance states were more correlated, and therefore closer to the exact energy value, than the B states were. This gave $1s2s^22p^3$ shape resonances in the ThII cross section that were unphysically much too low in energy (this same phenomenon existed in our earlier work on C^- [9]).

Both theoretical calculations were performed without the inclusion of any relativistic effects so that total orbital and spin angular momenta *L* and *S* are each conserved. Within our *R*-matrix approaches, these can be included as first order (in v^2/c^2) corrections such as the mass-velocity, Darwin, and spin-orbit effects [38,41]. Inclusion of spin-orbit effects, however, requires a recoupling to an alternate scheme since only *J* is a good quantum number, and this in turn leads to Breit-Pauli *R*-matrix computations [38,39] that are prohibitively complex when using the large CI description needed for this highly correlated system [42–45]. The B target energies we computed in the nonrelativistic ThI and ThII calculations, compared with experiment [46], are given in Table I. Also tabulated are the computed and measured [35] B^- energies relative to the ground B energy, and, after converting to photon energies, we found it more meaningful to apply a constant shift of our theoretical photon energies so that the $1s2s^22p^2(^4P)$ thresholds aligned at 188.63 as this gave the closest agreement between theoretical and experimental resonance energy positions (see below).

We have also performed ThII calculations, including mass-velocity, Darwin, and spin-orbit relativistic interactions, for the B target states and compare to ThII nonrelativistic and level-resolved experimental results, where available (see Table II). While these effects change the energies on the order of $\lesssim 0.01$ eV for full-*K*-shell states, relatively larger differences for the excitation energies to the *K*-shell-vacancy states—roughly 0.1 eV—are found, due primarily to the much larger velocities of $1s$ electrons compared to outer-shell electrons. However, this effect is found to be roughly the same between all singly and doubly excited B states and the *differences* between the important $1s2s^22p^2$ *K*-shell thresholds are still on the order of $\lesssim 0.01$ eV (see Table II), and since global shifts in photon energies are applied to both theoretical results anyway, we conclude that the final reported theoretical photodetachment cross sections vs photon energy, adjusted so that the $1s2s^22p^2(^4P)$ threshold is at 188.63 eV, is essentially unaffected by relativistic corrections. We therefore proceed with our much simpler nonrelativistic studies.

Referring back to the computed nonrelativistic energies in Table I, it is seen that the singly excited $1s^22s2p^2$ and $1s^22p^3$ states are not described accurately by the ThII calculations, for which the $1s$, $2s$, and $2p$ orbitals were optimized on the full *K*-shell $1s^22s^22p$ configuration, and the correlation $3s$, $3p$, and $3d$ pseudo-orbitals were optimized on the

TABLE I. Computed and measured bound energies of B^- and B (in eV).

	Relative to ground-state B			Theoretical photon energies		Shifted $1s2s^22p^3(^4S)$ to 188.63 eV	
LS term	ThI[a]	ThII[a]	Experiment	ThI[b]	ThII[b]	ThI[c]	ThII[c]
$1s^22s^22p^2(^3P)$	−0.276	−0.567	−0.280[d]	0.000	0.000	−0.128	−0.461
$1s^22s^22p(^2P)$	0.000	0.000	0.000	0.276	0.567	0.148	0.107
$1s^22s2p^2(^4P)$	3.545	3.391	3.579[e]	3.821	3.958	3.693	3.498
(^2D)	6.126	6.513	5.933[e]	6.402	7.080	6.274	6.620
(^2S)	7.871	9.023	7.880[e]	8.147	9.590	8.019	9.129
(^2P)	9.195	9.824	8.992[e]	9.471	10.392	9.343	9.931
$1s^22p^3(^4S)$	12.008	12.152	12.038[e]	12.284	12.720	12.156	12.259
(^2D)	12.167	13.197	12.374[e]	12.443	13.764	12.315	13.303
(^2P)	14.640	15.575	13.782[e]	14.916	16.143	14.788	15.682
$1s2s^22p^2(^4P)$	188.482	188.523		188.758	189.091	188.630	188.630
(^2D)	190.719	190.801		190.995	191.368	190.867	190.907
(^2P)	190.914	190.957		191.190	191.524	191.062	191.063
(^2S)	192.001	192.286		192.277	192.853	192.149	192.392
$1s2s2p^3(^4S)$	193.949	193.649		194.225	194.216	194.097	193.755
(^4D)	194.107	194.174		194.383	194.741	194.255	194.281
(^4P)	195.423	195.918		195.699	196.485	195.571	196.024
(^2D)	197.469	197.316		197.745	197.883	197.617	197.422
(^2P)	199.030	199.124		199.306	199.692	199.178	199.231
(^2D)	199.879	200.210		200.155	200.778	200.027	200.317
(^4S)	200.176	200.300		200.452	200.867	200.324	200.406
(^2S)	201.586	201.999		201.862	202.566	201.734	202.106
(^2P)	201.646	202.182		201.922	202.750	201.794	202.289
$1s2p^4(^4P)$	204.179	203.909		204.455	204.477	204.327	204.016
(^2D)	205.860	205.569		206.136	206.136	206.008	205.675
(^2P)	206.547	206.003		206.823	206.570	206.695	206.109
(^2S)	209.973	209.527		210.249	210.095	210.121	209.634

[a]Relative to B$[1s^22s^22p(^2P)]$, ThI and ThII unshifted.
[b]Photon energy relative to $B^-[1s^22s^22p^2(^3P)]$, ThI and ThII unshifted.
[c]Same as b, but ThI (ThII) shifted by −0.13 (−0.36) eV.
[d]Reference [35].
[e]Reference [46].

K-shell-vacancy $1s2s^22p^2$ configuration. This approach in the ThII method, which is obviated in the ThI method, for which every state is described using a separate, appropriate set of orbitals, does not adequately describe the states with a full 1*s* subshell but a 2*s* subshell with occupancy number of only one or zero.

We point out that Hund's rule [41,47], while obeyed in general for B configurations such as $1s^22p^3$ and $1s2s^22p^2$, is not true for the $1s^22s2p^2$ configuration since the ^2S term is lower in energy than the ^2P term. This somewhat counterintuitive behavior will also be seen for the B^- shape resonances in the next section when we compare our two theoretical results to the latest absolute experimental measurements. However, it should be noted that these same comparisons were performed using earlier experimental results for *K*-shell photodetachment of B^- [48,49]. In fact, results for *L*-shell photodetachment results were already presented [48] where excellent agreement with the available experiments [50,51] was found. From a purely angular momentum perspective, the $1s^22s2p^2$ *L*-edge is identical to the presently considered $1s2s^22p^2$ *K* edge, although the *dynamics* of the former are obviously different. Thus, the shape resonances seen near the $2s^{-1}$ threshold [48,51] are not the same as those near the $1s^{-1}$ threshold, as we shall see in the next section.

Last, it is seen in Table I that the ThII B^- binding energy of 0.567 eV is almost twice that of the ThI or experimental values. This is because we choose not to eliminate additional B^- configurations only in the B^- ground state symmetry (^3P). While we could do so, we have found that a more accurate description of the photodetachment dynamics is obtained when the largest CI description possible is used for the ground state, and the photon energy is adjusted accordingly. In the present case, the highly correlated B^- state is roughly 0.3 eV closer to the converged energy than is the *B* ground state, leading to an overestimate in the *relative* binding energy by this amount.

TABLE II. Computed ThII nonrelativistic (LS) and semirelativistic (IC) B energies compared to singly excited experimental [46] values. Also listed are the scaled differences $\Delta E \equiv E^{IC} - E^{LS} - 0.052$, where the 0.052 eV represents the average energy difference $\Sigma_{i=1}^{8}(E_i^{IC} - E_i^{LS})/8$ due to a relativistic shift between half-full-*K*-shell and full-*K*-shell energies for the important $1s2s^2 2p^2$ levels.

LS term	*J* level	LS	IC	NIST	ΔE
$1s^2 2s^2 2p(^2P)$	1/2	0.000	0.000	0.000	
	3/2		0.002	0.002	
$1s^2 2s 2p^2(^4P)$	1/2	3.391	3.396	3.580	
	3/2		3.397	3.580	
	5/2		3.398	3.581	
(^2D)	3/2	6.513	6.520	5.934	
	5/2		6.520	5.934	
(^2S)	1/2	9.023	9.030	7.881	
(^2P)	1/2	9.824	9.831	8.992	
	3/2		9.833	8.993	
$1s^2 2p^3(^4S)$	3/2	12.152	12.166	12.039	
(^2D)	3/2	13.197	13.211	12.374	
	5/2		13.211	12.374	
(^2P)	1/2	15.575	15.589	13.775	
	3/2		15.589	13.787	
$1s2s^2 2p^2(^4P)$	1/2	188.523	188.581		0.005
	3/2		188.582		0.007
	5/2		188.585		0.009
(^2D)	3/2	190.801	190.860		0.006
	5/2		190.860		0.007
(^2P)	1/2	190.957	191.013		0.004
	3/2		191.016		0.007
(^2S)	1/2	192.286	192.345		0.007
$1s2s2p^3(^4S)$	3/2	193.649	193.716		
(^4D)	1/2	194.174	194.242		
	3/2		194.242		
	5/2		194.242		
	7/2		194.243		
(^4P)	1/2	195.918	195.986		
	3/2		195.986		
	5/2		195.986		
(^2D)	3/2	197.316	197.384		
	5/2		197.384		
(^2P)	1/2	199.124	199.193		
	3/2		199.193		
(^2D)	3/2	200.210	200.281		
	5/2		200.281		
(^4S)	3/2	200.300	200.372		
(^2S)	1/2	201.999	202.069		
(^2P)	1/2	202.182	202.253		
	3/2		202.253		
$1s2p^4(^4P)$	5/2	203.909	203.988		
	3/2		203.990		
	1/2		203.991		
(^2D)	3/2	205.569	205.648		
	5/2		205.649		
(^2P)	3/2	206.003	206.081		
	1/2		206.084		
(^2S)	1/2	209.527	209.442		

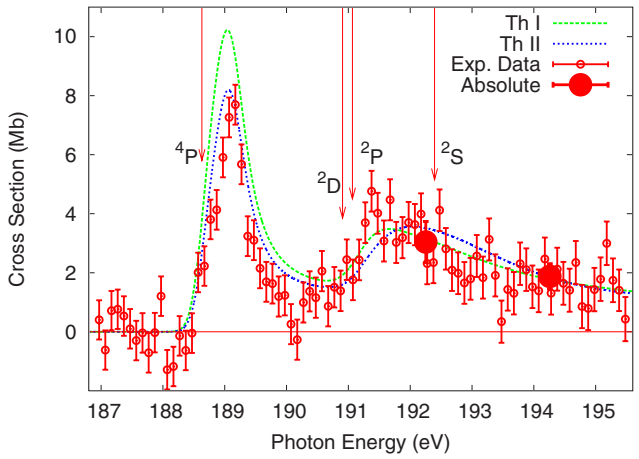

FIG. 1. (Color online) Lower-resolution (390 meV) detection of B^+ ions following *K*-shell photodetachment of B^- [see Eq. (1)] over a broad photon energy range. The open red circles are the experimental data while the two solid red circles are absolute cross section measurements used to calibrate the spectrum. The ThI (nonorthogonal basis, B-spline *R*-matrix results; long-dashed green curve) and ThII (orthogonal basis *R*-matrix results; short-dashed blue curve) convoluted (390 meV) results are also shown. The four vertical arrows show the positions of the four B^* $1s2s^22p^2$ (^4P,^2D,^2P,^2S) thresholds from the ThII calculations (both ThI and ThII results have been aligned such that the ^4P threshold energy is 188.63 eV).

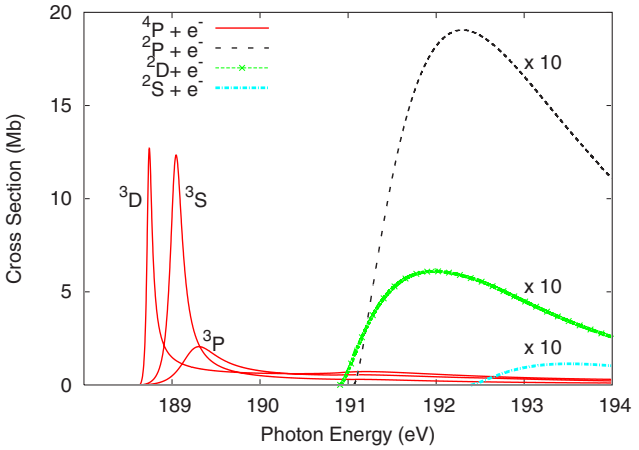

FIG. 2. (Color online) A partitioning, within the ThII calculations, of the photodetachment cross section in Eq. (1) into the ^4P (solid red), ^2P (dashed black), ^2D (green crosses), and ^2S (dashed-dotted cyan) channel contributions. The ^2D, ^2P, and ^2S channels have been magnified by a factor of 10 for clarity whereas the dominant ^4P channel has been further broken into the incoherent contributions from each of the three final ^3D, ^3P, and ^3S symmetries, indicating a separate shape resonance within each partial wave.

IV. RESULTS AND DISCUSSION

The experimental data generated from two different experimental runs are shown in Fig. 1. They depict the absolute cross section for 1*s* photodetachment of B^- as a function of a broad photon energy range (187–195 eV) at a resolution of 390 meV. The two filled circles represent absolute cross section measurements and all the other data (empty circles) shown in this figure have been scaled to these two points. The cross section at 192.25 eV is 3.04±0.70 Mb and corresponds to the average of five measurements while the one at 194.26 eV with a value of 1.88±0.43 Mb is the average of two measurements. Our uncertainty in the measurement of absolute cross sections is about 23% which is typical for merged ion-photon beam experiments [11–13].

We also show in Fig. 1 both *R*-matrix (ThI and ThII) results that have been further convoluted with a 390 meV Gaussian to simulate the photon bandwidth. Aside from the expected turn on of *K*-shell photodetachment at the $1s2s^22p^2$ (^4P) and $1s2s^22p^2$ (^2P) thresholds at about 188.6 and 191 eV, respectively, the only other striking feature observable at this level of resolution is an apparent resonance just above the $1s2s^22p^2$ (^4P) threshold at about 189 eV.

We can better understand the origin of these features by partitioning, within our theoretical treatment, the total cross section in Eq. (1) into the four partial cross sections for each channel $1s2s^22p^2$ (^4P,^2P,^2D,^2S)+e^-. These are shown in Fig. 2 (where the dominant and more interesting ^4P channel has been further broken into its three final symmetries ^3S, ^3P, and ^3D). We see that, as expected, the ^4P and ^2P channels dominate, with a somewhat smaller contribution from the ^2D channel and an even smaller contribution from the ^2S channel, both of which are populated via channel coupling with the ^2P channel (since the ^4P channel shows a slight increase near the ^2P threshold, it also seems to couple somewhat).

This channel coupling is enhanced in the ^2D channel compared to the ^2S channel not because of a closer degeneracy of the former target energy to the allowed ^2P channel compared to the latter [52]. Rather, the partial wave breakdown of each channel reveals that while the ^2D and ^2S channels each contribute approximately equal to the ^3P partial wave, the ^2D channel also contributes to the ^3D partial wave that is forbidden for the ^2S channel, and this contribution is roughly twice the ^3P contribution. In other words, the three possible final channels are: $1s2s^22p^2(^2S)\epsilon p(^3P)$,$1s2s^22p^2(^2D)\epsilon p(^3P)$, and $1s2s^22p^2(^2D)\epsilon p(^3D)$, with the last amplitude being nearly twice that of the (approximately equal) first two amplitudes.

Thus the second maximum observed in Fig. 1 at about 192 eV can now be understood, with the help of Fig. 2, as being composed of relatively featureless continuum, or *threshold* effects—the opening of the ^2P photodetachment channel together with weaker, coupled ^2D and ^2S channels. On the other hand, the first maximum in Fig. 1 at about 189 eV is now seen to be composed of three obvious $1s2s^22p^3$ ^3S, ^3P, and ^3D shape resonances with resonance positions relative to threshold (and therefore their widths) varying due to the geometrically different scattering potentials seen by the departing photoelectron.

It needs to be pointed out that, since the two *R*-matrix methods are based on a coupled-channel formalism, Auger decay to full *K*-shell B (the lowest eight states listed in Table I) is explicitly included, as is Auger decay to *K*-shell vacancy B^* (states nine and higher). However, since Eq. (1) indicates that only photodetachment to these latter, *K*-shell vacancy states leads to the observed B^+ production, our reported ThI and ThII results only include the sum of partial photodetach-

ment cross sections to states nine and higher. Thus, even though the first eight states are included in the calculation to best predict the resonance widths, etc., photodetachment to these same eight states (which can proceed through Auger decay of the three shape resonances, for instance) are *not* included in our reported theoretical results.

The particular ordering of the three shape resonances according to their *LS* values may seem counterintuitive in that Hund's rule [47,41] is not totally satisfied—the ^3S resonance is lower in energy than the ^3P resonance. However, upon studying, within a single-configuration approximation, the energies of the three $1s2s^22p^3$ *LS* states, we find that the difference is due to the angular factors that multiply only two Slater integrals [41], i.e.,

$$E(LS) = E_0 + c_1(LS)R^1(1s,2p;2p,1s) + c_2(LS)R^2(1s,2p;1s,2p), \tag{4}$$

where

$$R^\lambda(a,b;c,d) = \int dr \int dr' P_a(r)P_b(r')\frac{r_<^\lambda}{r_>^{\lambda+1}}P_c(r)P_d(r') \tag{5}$$

is the standard Slater integral [41], $P_a(r)$ is the radial orbital for electron a, $r_<$ ($r_>$) is the minimum (maximum) of r and r', and E_0 is the *LS*-independent energy contribution from several other Slater integrals. We note first of all that both the Slater integrals in Eq. (4) are positive since the $1s$ and $2p$ orbitals are nodeless. Second, we find that $c_1(^3P)=c_1(^3D)=-\frac{2}{3}$ whereas $c_2(^3P)=0$ but $c_2(^3D)=-\frac{6}{25}$. This second, negative contribution guarantees that $E(^3D)<E(^3P)$ as is seen in Fig. 2. On the other hand, $c_1(^3S)=+\frac{1}{3}$, which would tend to yield $E(^3S)>E(^3P)>E(^3D)$, thereby obeying Hund's rule. However, $c_2(^3S)=-\frac{1}{6}$, i.e., $c_2(^3S)<c_2(^3D)<c_2(^3P)$, and this results in a lowering of $E(^3S)$ relative to $E(^3P)$ and $E(^3D)$. The net result, which now depends on the *dynamics*—the relative strengths of the two (so-called exchange dipole and direct quadrupole) Slater integrals—as well as the angular coefficients c_1 and c_2—is that the ^3S resonance position lies in between the ^3D and ^3P resonances: $E(^3D)<E(^3S)<E(^3P)$, as is shown in Fig. 2, contrary to Hund's rule.

It should be pointed out that the direct and exchange electron-electron interactions are more important in negative ions due to the lack of a long-range monopole potential of the neutral atom seen by the outermost electron. It is the same reason why Hund's rule, which is empirically based on *neutral* atoms, where the direct and exchange dipole (and higher) contributions are typically perturbations rather than dominant, breaks down.

We find that these theoretical shape resonance features can be fitted extremely well by three Breit-Wigner resonance profiles with Wigner threshold law behavior. This suggests a fitting of our experimental data as a function of photon energy $E=h\nu$ using the sum of three modified resonance profiles with functional form as first suggested by Peterson *et al.* [53]:

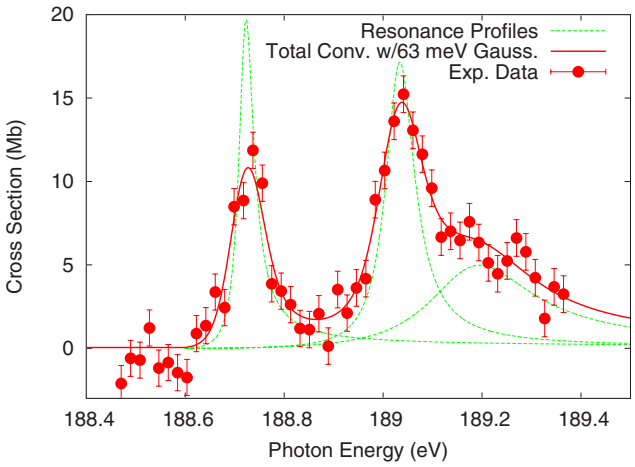

FIG. 3. (Color online) Experimental cross sections for *K*-shell photodetachment of B^- leading to B^+ over the photon energy range of the first structure shown in Fig. 1. Here, the three structures observed and fitted are the $1s2s^22p^3(^3D,^3S,^3P)$ shape resonances. The three resonance profiles are obtained based on fits using Eq. (6).

$$\sigma^{fit}(E) = \sum_{i=1}^{3} A_i \left[\frac{(E-E^{thr})}{(E_i^{res}-E^{thr})}\right]^{l+\frac{1}{2}} \frac{\Gamma_i/2\pi}{(E-E_i^{res})^2+(\Gamma_i/2)^2}. \tag{6}$$

Here E^{thr} is the $1s2s^22p^2(^4P)$ threshold energy, the orbital angular momentum takes the value of $l=1$ for our p-wave case, E_i^{res} are the energies of each of the three resonances, Γ_i are the three corresponding natural (Lorentzian) widths, and the A_i are three separate amplitude factors. We use this alternate form to normalize the second Wigner threshold term to unity on resonance ($E=E_i^{res}$) and to normalize the energy-integrated area under the third Lorentzian term to one, so that the amplitude A_i represents the effective photoabsorption strength, or area (in Mb-eV), of each $1s\rightarrow 2p$ shape resonance. This simple formula has shown excellent agreement to numerous p-wave shape resonances both in valence electron [2,53,54] and inner-shell photodetachment [18].

We show in Fig. 3 our higher resolution (63 meV) measurements in the near-threshold region. These data were scaled to the absolute cross section measurements, shown in Fig. 1, and are thus displayed as an approximate absolute cross section. The best-fit curve is shown in Fig. 3 as the red solid curve with the green dashed curves representing the three decomposed partial waves with spectral bandwidth effects removed. Assuming a common threshold position, a total of 10 parameters are required for fitting the experimental data to Eq. (6). In addition, because the observed spectrum is broadened significantly by the spectral resolution of the monochromator, the fitting function in Eq. (6) is further convoluted with a 63 meV Gaussian to simulate the spectral bandwidth. Allowing the bandwidth to vary as a fitting parameter yields an estimated bandwidth of 62 ± 34 meV, consistent with the expected bandwidth of 63 ± 3 meV given the width of the monochromator slits.

TABLE III. B^- $1s2s^22p^3$ shape resonance parameters. Experimental line positions include photon energy calibration uncertainty.

		ThI	ThII	Expt. fit
	E^{thr} (eV)	188.63[a]	188.63[a]	$188.6(^{+0.1}_{-0.2})$
(^3D)	E^{res} (eV)	188.73	188.73[b]	188.72±0.05
	Γ (eV)	0.056	0.071	0.037±0.020
	A (Mb-eV)	1.80	1.32	1.14±0.28
(^3S)	E^{res} (eV)	189.02	189.03[b]	189.03±0.05
	Γ(eV)	0.178	0.165	0.071±0.022
	A (Mb-eV)	4.00	3.10	1.92±0.48
(^3P)	E^{res} (eV)	189.22	189.22	189.17±0.13
	Γ (eV)	0.528	0.536	$0.26(^{+0.26}_{-0.10})$
	A (Mb-eV)	1.82	1.60	1.92±0.52

[a]Both theoretical results have been globally shifted in photon energy to give this same threshold value (see text).
[b]These two ThII resonances were artificially shifted by +0.1 eV relative to threshold (see text).

It is clearly seen that the resonance profiles, once convoluted with a 63 meV Gaussian, are in very good agreement with the measured cross section. By reducing our experimental cross section into a fit involving three separate partial wave contributions of modified resonance profile, we can use the separate, unconvoluted, experimentally inferred profiles to make a closer comparison with the two theoretical positions, natural (Lorentzian) widths, and strength parameters (areas) of each shape resonance. The best-fit parameters returned for the threshold positions and resonance parameters, along with estimated total uncertainties, are listed in Table III and compared to the theoretically determined values (all errors are quoted to 1 standard deviation throughout).

For the theoretical positions and widths, rather than fitting to our photodetachment cross sections, we instead fit to the trace of Smith's time delay matrix Q [55], which near a resonance takes a Lorentzian form

$$tr(Q) = tr(iSdS^{\dagger}/dE) = \frac{\Gamma}{(E - E^{res})^2 + (\Gamma/2)^2}, \qquad (7)$$

where S is the computed scattering matrix that is block-diagonal with respect to the three separate partial waves ^3D, ^3S, and ^3P. This trace is not obscured by threshold or interference effects and is essentially a pure Lorentzian profile with a maximum of $4/\Gamma$ at $E=E^{res}$ from which the theoretical resonance positions and widths are easily and accurately determined. Given these accurate positions and widths, we then fit our computed cross section for each partial wave to the functional form of Eq. (6) to obtain the strengths (or areas) A_i.

Of the three calculated parameters—the position, width, and strength—the least accurate is typically the overall position as given by the $1s \rightarrow 2p$ photon energy between the B^- $1s^22s^22p^2$ ground state and the B^{-*} $1s2s^22p^3$ shape-resonance state. Therefore, in order to align photon energies between the experimentally inferred and theoretically determined *thresholds*, we applied global shifts in total photon energies by −0.13 eV for the ThI results and by −0.36 eV for the ThII results in order that both theoretical $1s2s^22p^2(^4P)$ thresholds are shifted to 188.63 eV—consistent with the experimentally inferred value of $188.6(^{+0.1}_{-0.2})$ (see Table III).

It is immediately evident that the ThII results require a much larger global shift in photon energy in order to align the threshold properties. This is primarily due to the overly converged energy of the B^- $1s^22s^22p^2$ state, relative to the B and B^* states, by −0.277 eV, when using the ThII orthogonal basis, as discussed above. But even the ThII ^3D and ^3P shape resonance positions, *relative* to the $1s2s^22p^2$ threshold positions, were initially found to be about 0.1 eV *lower* than that observed (or calculated by ThI); this was especially problematic for the ^3D resonance since it initially straddled threshold. We therefore artificially shifted the ThII $1s2s^22p^3$ shape resonances by +0.1 eV *relative* to the $1s2s^22p^2(^4P)$ threshold in order to give correct relative resonance positions (including an *above-threshold* ^3D position) for better comparison of resonance widths and strengths.

A comparison between our individual experimental fits and the two R-matrix results, resolved into each final partial wave, is shown in Fig. 4, and the various extracted resonance parameters are listed in Table III. We note that the resonance strengths A in Table III do not behave as would be expected based on statistical weighting $(2S+1)(2L+1)$ alone. Rather, as is the case in general [56], the relative probabilities are complicated expressions derived from Racah algebra and only reduce to (LS) statistical probabilities under certain averaging procedures. For the present case of photoexcitation from one LS term (^3P) of the $1s^22s^22p^2$ configuration leading to three separate LS terms of the $1s2s^22p^3$ configuration, statistical weighting is not obeyed.

We first address the computed and inferred resonance positions. Any computational error in a resonance position can affect the resultant widths and/or strengths in two ways, because (i) the shape-resonance width varies as approximately $(E-E^{thr})^{3/2}$ [53] so resonances predicted to be too high (low) in energy relative to threshold will have widths that are unphysically too small (large), and (ii) a resonance that straddles threshold (or indeed falls below threshold) contributes only partially (or not at all) to the K-shell-excited channels. This is why the ThII results were artificially shifted relative to threshold—to filter out these dynamic threshold effects on the final computed cross section. Thus the ThII resonance positions, as described above, are seen to be inaccurate both in absolute photon energy by ≈0.4 eV and in relative energy by perhaps ≈0.1 eV. On the other hand, the more reliable ThI positions were shifted by only 0.1 eV—still twice the estimated experimental uncertainty. Once this shift of 0.1 eV, whose value was determined by aligning all the resonance features, was applied, the ThI ^3D and ^3S resonance positions were found to be in quite good agreement with the experimentally inferred values, as seen in Table III. In fact, the experimentally determined *differences* in resonance positions have smaller uncertainties since the overall photon energy calibration uncertainty is eliminated, and we obtain experimental differences (in eV) of $^3S-^3D=0.313\pm0.013$, $^3P-^3D=0.46\pm0.08$, and $^3P-^3S$

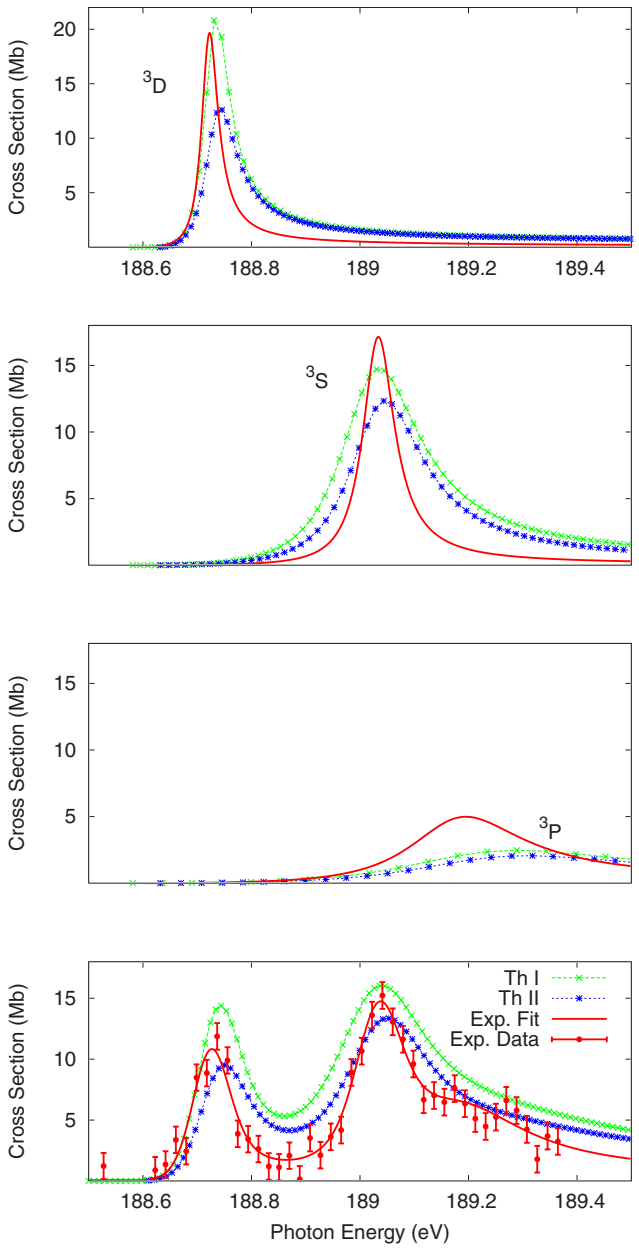

FIG. 4. (Color online) Partial and total cross sections for photodetachment of B^- leading to B^+. The experimentally inferred resonance profiles (solid red lines) and theoretical results (green crosses for ThI results, blue squares for ThII results) are shown for (top to bottom) the ^3D, ^3S, and ^3P symmetries followed by the summed, convoluted (with 63 meV Gaussians) cross sections.

$=0.14\pm0.09$, compared to the ThI values of 0.29, 0.49, and 0.20, all within about one standard deviation.

The experimentally inferred ^3P position has the largest energy uncertainty of the three resonances and is determined to be 189.17 eV, or 0.08 eV lower than the ThI value. This is mainly because the higher-resolution experimental data cover only the energy region $h\nu \leq 189.36$ eV, which roughly equals the ThI resonance *position*. Thus, the right half of the resonance, as predicted by ThI, is absent in the experimental data and could tend to favor a fit ^3P resonance position towards a lower energy. The absence of higher-energy experimental data also increases the uncertainty in the experimental resonance width. There is also a large uncertainty in the narrow ^3D experimental width of 0.037 eV due to the masking effect of the broader 63 meV spectral bandwidth used in the experiment. Given these rather large uncertainties, the ThI widths for the ^3D and ^3P resonances are in agreement with the experimental values.

However, the ThI ^3S resonance width is several standard deviations greater than the experimentally inferred width, and there seems to be no way to explain this rather large theoretical overestimate (by a factor of 2.5). Likewise, the ThI strengths A_i for the ^3S and ^3D resonances are greater than the experimental values by factors of 2 and 1.5, respectively. The ^3P resonance strengths are in fairly good agreement, although, again, due to the limited experimental energy range, the strength carries a large uncertainty. Regardless, there is an overall discrepancy by as much as a factor of 2 between the theoretical and experimental absolute energy-integrated cross sections that we cannot account for.

As a final note, we address the phenomenon of photoelectron-recapture due to post-collision interaction (PCI) effects [57,58]. Inner-shell photodetachment experiments that measure the resulting positively charged ion do not detect such recaptured states. For instance, in *K*-shell photodetachment of Li^-, where Auger decay of the *K*-shell vacancy Li^{**} state yields the Li^+ final states that are detected in the experiment, there is a probability, which is unity at threshold but quickly drops to zero away from threshold, that the slower photoelectron can be recaptured, yielding a neutral Li atom that will not be detected:

$$h\nu + 1s^2 2s^2(^1S) \rightarrow 1s2s^2(^2S)\epsilon p(^1P)$$

$$\downarrow$$

$$1s^2 \epsilon s \epsilon p$$

$$\swarrow \qquad \searrow$$

$$[\mathrm{Li}^+(1s^2)]\ \epsilon p \epsilon s \qquad [\mathrm{Li}(1s^2 np)]\ \epsilon s$$

double detachment PCI recapture

By considering the reduction in detected Li^+ ions because of the alternate recapture channel yielding neutral Li atoms, the strong $1s2s^22p(^1P)$ shape resonance just above the $1s2s^2(^2S)$ threshold was found to be much weaker than when this PCI effect was neglected [26].

However, for photodetachment of B^- (as with C^- [9,18]), PCI recapture effects are found to be negligible for the following reason: even if recapture does occur, only doubly excited B^{**} states remain following the departure of the intermediate Auger electron, and this doubly excited state undergoes a second Auger decay, yielding a B^+ ion anyway. Specifically, if the photodetachment process in Eq. (1) is extended to include the possibility of PCI recapture in the Auger process,

$$
\begin{array}{c}
1s2s^2 2p^2\,(^4P)\,\epsilon p \\
\downarrow \\
1s^2 2l2l'\epsilon l\,(^4P)\,\epsilon p
\end{array}
\tag{8}
$$

$$
\begin{array}{ll}
\swarrow & \searrow \\
\left[\mathrm{B}^+(1s^2 2l2l')\right]\epsilon p\epsilon l & \left[\mathrm{B}(1s^2 2l2l' np)\right]\epsilon l \\
\text{double detachment} & \text{PCI recapture} \\
 & \downarrow \\
 & \left[\mathrm{B}^+(1s^2 2s^2)\epsilon l_2\right]\epsilon l \\
 & \text{double detachment}
\end{array}
\tag{9}
$$

we see that the possible final states following the initial Auger process $(8 \rightarrow 9)$ are limited to the $1s^2 2l2l'\epsilon l(^4P)$ states which, due to spin conservation, cannot include the $1s^2 2s^2(^1S)\epsilon l$ continua. Therefore, only the $1s^2 2s2pnp$ and $1s^2 2p^2 np$ recaptured states can be populated, and essentially all of these lie above the $1s^2 2s^2\epsilon l_2$ continuum, i.e., they are autoionizing and will eventually yield B^+ ions, which are detected, and two Auger electrons ϵl_2 and ϵl. Therefore, no further PCI reduction of the theoretical cross sections was necessary in order to simulate the measured B^+ yield.

V. CONCLUSION

The present work has explored experimentally and theoretically the *K*-shell photodetachment of a light negative ion, B^-. The experiment was able to provide absolute cross sections that could then be compared directly to two separate, somewhat different *R*-matrix calculations. A detailed analysis of the spectrum reveals three near-threshold shape resonances that are each accurately described by a combination of Wigner-threshold and Breit-Wigner Lorentzian resonance profiles.

The main difference between our two *R*-matrix approaches is that the ThI method is tailored to use a sufficiently large, separate basis of orbitals for *each* of the initial B^-, intermediate B^{-*}, and residual B and B^* (plus a free electron) states—a so-called nonorthogonal basis approach. The ThI results are in very good agreement with the experimentally observed spectrum except for a disturbing, unresolved discrepancy, by several standard deviations between the theoretically predicted and measured widths for the $1s2s^2 2p^3(^3S)$ shape resonance and by as much as a factor of 2 in the energy-integrated resonance cross sections. The ThII method, being limited to the use of the *same* orthogonal basis to describe each of the initial, intermediate, and final states, is clearly a less accurate description of the photodetachment process in question, yielding resonance energy positions, in particular, that are unphysical. Further convergence of the ThII calculations would require additional consideration of $4l$ and $5l$ orbitals and the accompanying single- and double-promotional configuration-interaction expansions, which leads to a tremendously more complicated computation. And since the overall qualitative agreement between ThII and either ThI or experiment, for the most part, seems sufficient, we choose not to pursue further ThII convergence.

Our measurements provide the total cross section which does not allow direct, detailed understanding of the measured features. Nevertheless, we have ruled out the possibility of post-collision photoelectron recapture, which otherwise would require a modification of the computed cross sections to reproduce the actual near-threshold B^+ positive ion yield. In the future, more intense photon sources and higher resolution photoelectron spectroscopy experiments that measure the partial cross sections will allow better quantitative comparisons between theory and experiment.

ACKNOWLEDGMENTS

This work was supported by DoE, Office of Science, BES, Chemical, Geoscience and Biological Divisions. The ALS is funded by DoE, Scientific User Facilities Division. N.D.G. and C.W.W. were supported in part by the National Science Foundation under Grant Nos. 0140233 and 0456916. T.W.G. was supported in part by NASA's APRA and SHP SR&T programs.

[1] T. Andersen, H. K. Haugen, and H. Hotop, J. Phys. Chem. Ref. Data **28**, 1511 (1999), and references therein.
[2] S. J. Buckman and C. W. Clark, Rev. Mod. Phys. **66**, 539 (1994), and references therein.
[3] T. Andersen, Phys. Rep. **394**, 157 (2004).
[4] H. Kjeldsen, P. Andersen, F. Kristensen, and T. J. Andersen, J. Phys. B **34**, L353 (2001).
[5] N. Berrah, J. D. Bozek, A. A. Wills, G. Turri, H.-L. Zhou, S. T. Manson, G. Akerman, B. Rude, N. D. Gibson, C. W. Walter, L. Vo Ky, A. Hibbert, and S. M. Ferguson, Phys. Rev. Lett. **87**, 253002 (2001), and references therein.
[6] A. M. Covington, A. Aguilar, V. T. Davis, I. Alvarez, H. C. Bryant, C. Cisneros, M. Halka, D. Hanstorp, G. Hinojosa, A. S. Schlachter, J. S. Thompson, and D. J. Pegg, J. Phys. B **34**, L735 (2001).
[7] H. Kjeldsen, P. Andersen, F. Folkmann, J. E. Hansen, M. Kitajima, and T. Andersen, J. Phys. B **35**, 2845 (2002).
[8] N. Berrah, J. D. Bozek, G. Turri, G. Akerman, B. Rude, H. L. Zhou, and S. T. Manson, Phys. Rev. Lett. **88**, 093001 (2002).
[9] N. D. Gibson, C. W. Walter, O. Zatsarinny, T. W. Gorczyca, G. D. Akerman, J. D. Bozek, M. Martins, B. M. McLaughlin, and N. Berrah, Phys. Rev. A **67**, 030703(R) (2003).
[10] N. Berrah, R. C. Bilodeau, G. D. Ackerman, J. D. Bozek, G. Turri, B. Rude, N. D. Gibson, C. W. Walter, and A. Aguilar, Phys. Scr., T **T 110**, 51 (2004).
[11] H. Kjeldsen, F. Folkmann, T. S. Jacobsen, and J. B. West, Phys. Rev. A **69**, 050501(R) (2004).
[12] A. Aguilar, J. S. Thompson, D. Calabrese, A. M. Covington, C. Cisneros, V. T. Davis, M. S. Gulley, M. Halka, D. Hanstorp, J. Sandström, B. M. McLaughlin, and D. J. Pegg, Phys. Rev. A **69**, 022711 (2004).
[13] R. C. Bilodeau, J. D. Bozek, A. Aguilar, G. D. Ackerman, G. Turri, and N. Berrah, Phys. Rev. Lett. **93**, 193001 (2004).
[14] V. T. Davis, A. Aguilar, A. M. Covington, J. S. Thompson, D. Calabrese, C. Cisneros, M. S. Gulley, M. Halka, D. Hanstorp, J. Sandström, B. M. McLaughlin, G. F. Gribakin, and D. J. Pegg, J. Phys. B **38**, 2579 (2005).
[15] R. C. Bilodeau, J. D. Bozek, N. D. Gibson, C. W. Walter, G. D. Ackerman, I. Dumitriu, and N. Berrah, Phys. Rev. Lett. **95**, 083001 (2005)
[16] R. C. Bilodeau, N. D. Gibson, J. D. Bozek, C. W. Walter, G. D. Ackerman, P. Andersson, J. G. Heredia, M. Perri, and N. Berrah, Phys. Rev. A **72**, 050701(R) (2005).
[17] J. Sandström, I. Alvarez, D. Calabrese, C. Cisneros, A. M. Covington, V. T. Davis, M. S. Gulley, M. Halka, D. Hanstorp, F. S. Schlachter, J. S. Thompson, and D. J. Pegg, Phys. Rev. A **72**, 034702 (2005).
[18] C. W. Walter, N. D. Gibson, R. C. Bilodeau, N. Berrah, J. D. Bozek, G. D. Ackerman, and A. Aguilar, Phys. Rev. A **73**, 062702 (2006).
[19] J. Xi and C. F. Fischer, Phys. Rev. A **59**, 307 (1999).
[20] H.-L. Zhou, S. T. Manson, L. Vo Ky, N. Feautrier, and A. Hibbert, Phys. Rev. Lett. **87**, 023001 (2001), and references therein.
[21] J. L. Sanz-Vicario, E. Lindroth, and N. Brandefelt, Phys. Rev. A **66**, 052713 (2002).
[22] O. Zatsarinny, T. W. Gorczyca, and C. J. Froese-Fisher, J. Phys. B **35**, 4161 (2002).
[23] J. L. Sanz-Vicario and E. Lindroth, Phys. Rev. A **65**, 060703(R) (2002).
[24] J. L. Sanz-Vicario, E. Lindroth, and N. Brandefelt, Phys. Rev. A **66**, 052713 (2002).
[25] H.-L. Zhou, S. T. Manson, L. Vo Ky, A. Hibbert, and N. Feautrier, Phys. Rev. A **64**, 012714 (2001).
[26] T. W. Gorczyca, O. Zatsarinny, H.-L. Zhou, S. T. Manson, Z. Felfli, and A. Z. Msezane, Phys. Rev. A **68**, 050703(R) (2003).
[27] G. Y. Kashenock and V. K. Ivanov, J. Phys. B **39**, 1379 (2006).
[28] H. Kjeldsen, J. Phys. B **39**, R235 (2006).
[29] A. M. Covington, A. Aguilar, I. R. Covington, M. F. Gharaibeh, G. Hinojosa, C. A. Shirley, R. A. Phaneuf, I. Álvarez, C. Cisneros, I. Dominguez-Lopez, M. M. SantAnna, A. S. Schlachter, B. M. McLaughlin, and A. Dalgarno, Phys. Rev. A **66**, 062710 (2002).
[30] R. D. Rathmell and G. A. Norton, Nucl. Instrum. Methods Phys. Res. B **21**, 270 (1987).
[31] G. C. King, M. Tronc, F. H. Read, and R. C. Bradford, J. Phys. B **10**, 2479 (1977).
[32] E. Hudson, D. A. Shirley, M. Domke, G. Remmers, A. Puschmann, T. Mandel, C. Xue, and G. Kaindl, Phys. Rev. A **47**, 361 (1993).
[33] O. Zatsarinny, Comput. Phys. Commun. **174**, 273 (2006).
[34] C. Froese Fischer, Comput. Phys. Commun. **64**, 369 (1990).
[35] M. Scheer, R. C. Bilodeau, and H. K. Haugen, Phys. Rev. Lett. **80**, 2562 (1998).
[36] C. Bloch, Nucl. Phys. **4**, 503 (1957).
[37] M. A. Crees, Comput. Phys. Commun. **19**, 103 (1980).
[38] P. G. Burke and K. A. Berrington, *Atomic Molecular Processes: An R-matrix Approach* (IOP, Bristol, 1993).
[39] K. A. Berrington, W. B. Eissner, and P. H. Norrington, Comput. Phys. Commun. **92**, 290 (1995).
[40] T. W. Gorczyca, F. Robicheaux, M. S. Pindzola, D. C. Griffin, and N. R. Badnell, Phys. Rev. A **52**, 3877 (1995).
[41] R. D. Cowan, *The Theory of Atomic Structure and Spectra* (University of California Press, Berkeley, CA, 1981).
[42] M. Aymar, C. H. Greene, and E. Luc-Koenig, Rev. Mod. Phys. **68**, 1015 (1996).
[43] T. W. Gorczyca, Z. Felfli, H.-L. Zhou, and S. T. Manson, Phys. Rev. A **58**, 3661 (1998).
[44] T. W. Gorczyca, Z. Felfli, N. C. Deb, and A. Z. Msezane, Phys. Rev. A **63**, 010702(R) (2000).
[45] Z. Felfli, T. W. Gorczyca, N. C. Deb, and A. Z. Msezane, Phys. Rev. A **66**, 042716 (2002).
[46] http://physics.nist.gov/cgibin/AtData/main-asd
[47] F. Hund, *Linienspektren und periodisches System der Elemente* (Julius Springer, Berlin, 1927), p. 124.
[48] O. Zatsarinny and T. W. Gorczyca, in XXIIIrd International Conference on Photonic, Electronic, and Atomic Collisions (ICPEAC 2003), Stockholm, Sweden, July 23-29, 2003; in Abstracts of contributed papers, http://atomlx04.physto.se/~icpeac/webpdffiles/Th006.pdf
[49] T. W. Gorczyca, Radiat. Phys. Chem. **70**, 407 (2004).
[50] D. H. Lee, C. Y. Tang, J. S. Thompson, W. D. Brandon, U. Ljungblad, D. Hanstorp, D. J. Pegg, J. Dellwo, and G. D. Alton, Phys. Rev. A **51**, 4284 (1995).
[51] P. Kristensen, H. H. Andersen, P. Balling, L. D. Steele, and T. Andersen, Phys. Rev. A **52**, 2847 (1995).
[52] We thank one referee of an earlier version of this manuscript for suggesting that perhaps the relative strengths of the channel magnitudes were due to other factors rather than the nearer degeneracy of the ^2D and ^2P channels.

[53] J. R. Peterson, Y. K. Bae, and D. L. Huestis, Phys. Rev. Lett. **55**, 692 (1985).

[54] C. W. Walter, J. A. Seifert, and J. R. Peterson, Phys. Rev. A **50**, 2257 (1994); C. W. Walter and J. R. Peterson, Phys. Rev. Lett. **68**, 2281 (1992); R. C. Bilodeau and H. K. Haugen, *ibid.* **85**, 534 (2000).

[55] F. T. Smith, Phys. Rev. **118**, 349 (1960).

[56] A. R. P. Rau, in *Electron and Photon Interactions with Atoms*, edited by H. Kleinpoppen and M. R. C. McDowell (Plenum, New York, 1976), p. 141.

[57] A. Russek and W. Mehlhorn, J. Phys. B **19**, 911 (1986), and references therein.

[58] G. B. Armen and J. C. Levin, Phys. Rev. A **56**, 3734 (1997), and references therein.